NANO · MICRO small
www.small-journal.com

Band Structure Engineering Promotes Anionic Redox Reversibility of Cobalt-Free Li-Rich Layered Oxides Cathodes

Xianggang Gao, Juanlang Guo, Shihao Li, Haiyan Zhang, Yi Zhang, Chaohong Guan, Mengran Wang, Yanqing Lai,* and Zhian Zhang**

Li-rich layered oxides cathodes (LLOs) have prevailed as the promising high-energy-density cathode materials due to their distinctive anionic redox chemistry. However, uncontrollable anionic redox process usually leads to structural deterioration and electrochemical degradation. Herein, a Mo/Cl co-doping strategy is proposed to regulate the relative position of energy band for modulating the anionic redox chemistry and strengthening the structural stability of Co-free $Li_{1.16}Mn_{0.56}Ni_{0.28}O_2$ cathodes. The incorporation of Mo with high d state orbit and Cl with low electronegativity can narrow the band energy gap between bonding and antibonding bands via increasing the filled lower-Hubbard band (LHB) and decreasing the non-bonding O 2p energy bands, promoting the anionic redox reversibility. In addition, strong covalent Mo—O and Mn—Cl bonding further increases the covalency of Mn—O band to further stabilize the O_2^{n-} species and enhance the reversible distortion of MnO_6 octahedron. The strengthening electronic conductivity, together with the epitaxial structure Li_2MoO_4 facilitates the fast Li^+ kinetics. As a result, the dual doping material exhibits enhanced anionic redox reversibility and suppressed oxygen release with increased cyclic stability and excellent rate performance. This strategy provides some guidance to design high-energy-density LLOs with desirable anionic redox reversibility and stable crystal structure via band structure engineering.

1. Introduction

The growing energy storage technology and electric mobility market have required the development of lithium-ion batteries (LIBs) with high energy density and low cost.[1] The capacity of cathode materials plays an important role in the innovations of high-energy-density LIBs.[2] Compared with commercialized cathode materials, Li-rich layered oxide cathodes (LLOs) can provide ultrahigh capacity due to the participation of anionic redox chemistry in the charge compensation.[3] However, the irreversible oxygen evolution also causes notorious oxygen release and structural deterioration, leading to the degradation of electrochemical performance.[4] It has been widely accepted that the unique Li—O—Li configurations in Li_2MnO_3 phase result in the formation of non-bonding O 2p orbitals and labile electrons, which promote the lattice oxygen to participate in the charge compensation at high voltage.[5] Although the non-bonding O 2p orbital theory has perfectly illustrated the anionic redox phenomenon, the reversibility of anionic redox and subsequent oxygen evolution fail to be clarified in this theory. Therefore, it is worthwhile to further enrich the anionic redox mechanism for guiding the focused modulation of anionic redox reversibility.

Actually, the cationic and anionic redox mechanism of layered oxides cathodes can be explained according to the characteristics of band structure as shown in **Scheme 1**. The band structure of conventional layered oxides cathodes like $LiCoO_2$, $LiNi_xMn_yCo_zO_2$ ($x + y + z = 1$) materials is considered to the orbital overlaps between the transition-metal (M) 3d orbitals and O 2p orbitals, contributing to the formation of bonding (M—O) and antibonding (M—O)* bands (Scheme 1a). Therefore, the redox process of these cathodes only involves the exchange of electrons from the (M—O)* bands, referring to the cationic redox chemistry. However, the band structure of LLOs also includes the weakly bonded O 2p orbitals with Li 2s orbitals resulting in the formation of the above-mentioned non-bonding O 2p bands except for the M—O bonds (Scheme 1b). The electrons can be removed from both the (M—O)* and non-bonding O 2p bands, existing the competitive cationic and anionic redox process.[6] The partially filled (M—O)* bands can be further split into the empty upper and filled lower-Hubbard bands (UHB and LHB, respectively). Therefore, the anionic redox can be specifically associated with the relative position of the LHB and non-bonding O 2p bands.[7] The comparison of the electron repulsion within d

X. Gao, J. Guo, S. Li, H. Zhang, Y. Zhang, M. Wang, Y. Lai, Z. Zhang
School of Metallurgy and Environment
Hunan Province Key Laboratory of Nonferrous Value-Added Metallurgy
Engineering Research Center of the Ministry of Education for Advanced Battery Materials
Central South University
Changsha, Hunan 410083, P. R. China
E-mail: mengranwang@csu.edu.cn; laiyanqing@csu.edu.cn; zhangzhian@csu.edu.cn

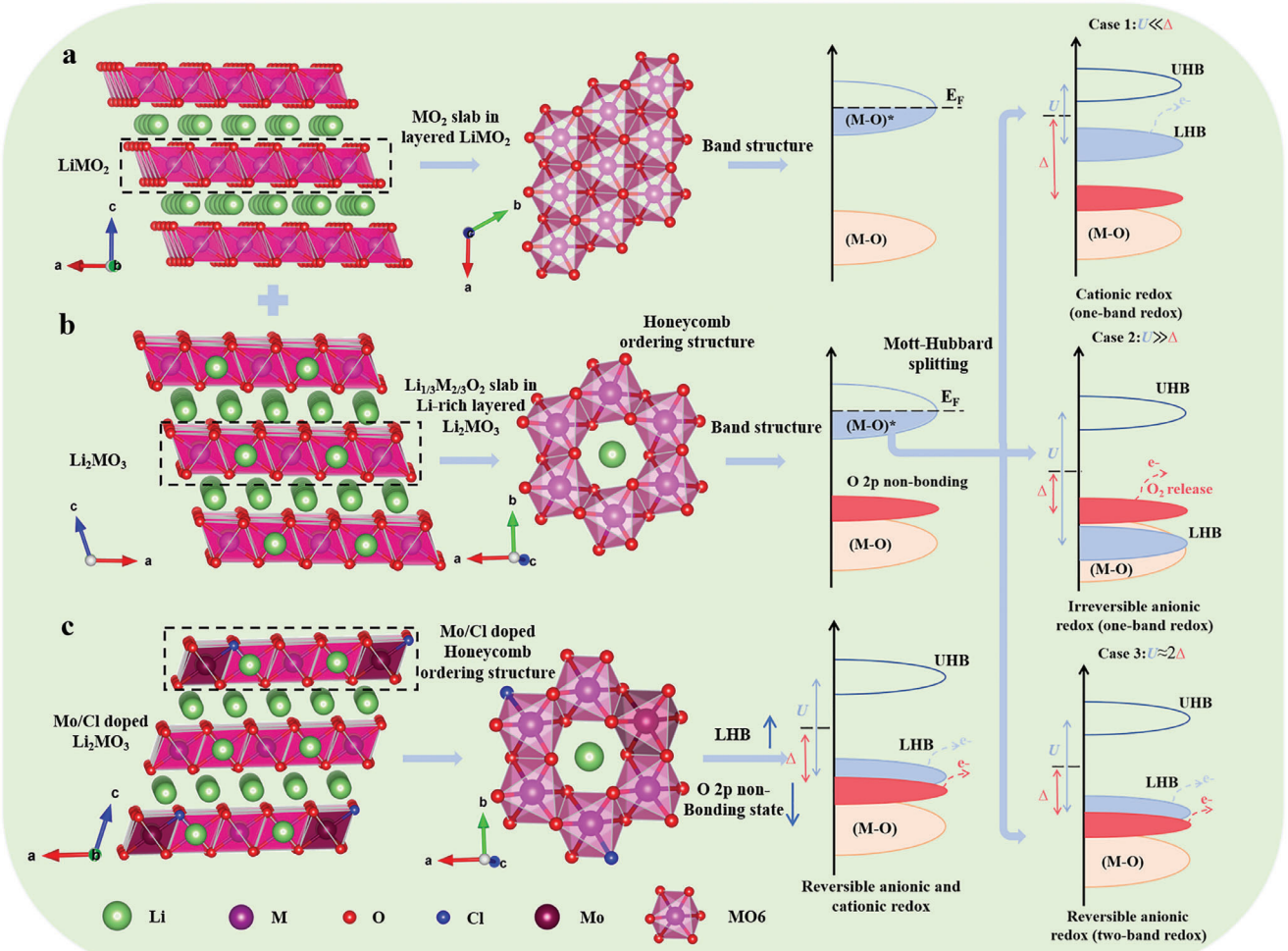
H. Zhang
Hunan ChangYuan LiCo Co., Ltd
Changsha, Hunan 410205, P. R. China

C. Guan
University of Michigan-Shanghai Jiao Tong University Joint Institute
Shanghai Jiao Tong University
800 Dongchuan Road, Shanghai 200240, P. R. China

The ORCID identification number(s) for the author(s) of this article can be found under https://doi.org/10.1002/smll.202401132

DOI: 10.1002/smll.202401132

 © 2024 Wiley-VCH GmbH



Scheme 1. Illustration of the crystal structures, band structure of layered oxides cathodes, and the regulation mechanism of anionic redox from the perspective of energy band: (a) The comparison of the crystal structures and band structures of (a) $LiMO_2$, (b) Li_2MO_3 and (c) Mo/Cl doped Li_2MO_3 layered oxides. The anionic redox mechanism is reflected according to the Mott-Hubbard splitting of Li_2MO_3 band structures: The relevant effect of the relationship between d-d Coulomb repulsion term U and charge transfer term Δ on anionic redox reversibility.

orbital (U) and charge transfer energy between central cation and ligand (Δ) can be applied to reflect the anionic redox activity[8]. When the $U \ll \Delta$ case, electrons are removed from the filled LHB bands experiencing the cationic redox. On the contrary ($U \gg \Delta$), electrons are exchanged from the non-bonding O 2p bands resulting in irreversible anionic redox and oxygen release. In the middle case ($U \approx 2\Delta$), the LHB bands can overlap the non-bonding O 2p bands, contributing to the simultaneous cationic and anionic redox reversibility. Therefore, it is critical to appropriately narrow the energy band gap between the term U and Δ of LLOs via the relative position modulation of the LHB and non-bonding O 2p energy bands and finally achieve the enhanced anionic redox reversibility.

Given the above considerations, we propose a Mo/Cl co-doping strategy to regulate the relative position of energy band for realizing the reversible exchange electrons from both the non-bonding O 2p and antibonding (M—O)* bands. The high d state Mo substitution with low d orbital coulombic interaction increases the position of LHB band and decrease the non-bonding O 2p band energy, contributing to narrow the band gap between for realizing the intermediate case $U \approx 2\Delta$ with reversible anionic redox (Scheme 1c). The formation of strong covalent Mo—O bonding, together with the low electronegative Cl substitution further increase the covalency of Mn—O bond, which is beneficial for stabilizing the O_2^{n-} species and strengthening the reversible distortion of MnO_6 octahedron. In addition, the strong Mo—O and Mn—Cl bonds also increase the oxygen vacancy formation energy and suppress the oxygen release. What is more, the strengthening electronic conductivity and epitaxial Li_2MoO_4 structure on the surface further facilitate the fast Li^+ kinetics and alleviate the interfacial side reactions. As a result, the co-doping materials show increasing capacity retention and slow voltage decay after long-term cycling due to the enhanced anionic redox reversibility and structural stability.

© 2024 Wiley-VCH GmbH

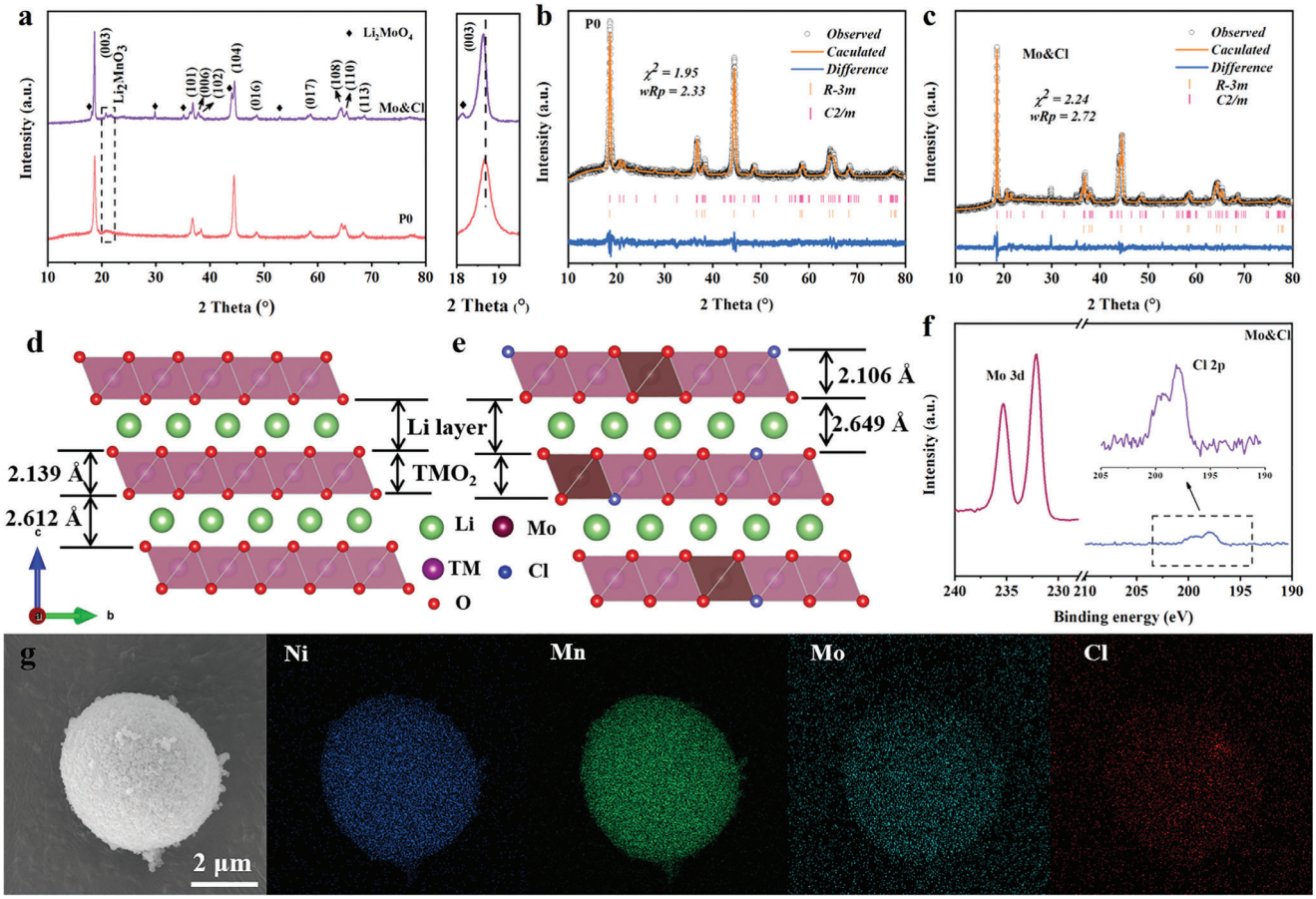


Figure 1. a) XRD patterns and corresponding (003) peaks of P0 and Mo&Cl materials. Two-phase model Rietveld refinement of b) P0 and c) Mo&Cl materials. Crystal structure and interslab spacing of the Li layer and TM layer for d) P0 and e) Mo and Cl materials. f) XPS spectra of Mo 3d and Cl 2p for Mo&Cl materials. g) SEM image and the corresponding EDS mapping of Mo&Cl materials.

2. Results and Discussion

The pristine and Mo/Cl co-doped materials are marked as P0 and Mo&Cl materials, respectively. First, the powered XRD was applied to detect the influence of Mo/Cl co-doping on the crystal structure of the materials (**Figure 1a**). The main diffraction peaks of P0 and Mo&Cl materials correspond to the characteristic of $LiMO_2$ phase with α-$NaFeO_2$ structure (space group: *R-3m*). Besides, some weak diffractions appear at 20°–25°, demonstrating the existence of layered Li_2MnO_3 phase (space group *C2/m*) as composite structure at nanoscale.[9] In addition, the well splitting of (006)/(102) and (108)/(110) peaks demonstrate the well-ordered layered structure for all the materials.[10] However, some new weak peaks can be observed at the XRD spectra of Mo&Cl material in comparison with P0 material. It is firstly presumed to be the Li_2MoO_4 phase with the spinel-like structure according to the previous report.[11] The molten MoO_3 at high temperature can deplete partial surface lithium to form the Li_2MoO_4 phase. In order to further demonstrate the reasonable formation mechanisms of the aforementioned species, the crystal structural changes of single Mo and Cl doping materials are separately analyzed via XRD test (Figure S1, Supporting Information). Similar new peaks appear after individual Mo doping and its signals become obvious with the increasing usage of MoO_3 (Figure S1a, Supporting Information). However, no additional peaks can be detected after the sole Cl doping (Figure S1b, Supporting Information), proving the fact that the generation of Li_2MoO_4 phase is ascribed to the introduction of Mo element. What is more, the position of (003) peaks of both the Mo/Cl co-doping and individual Mo or Cl doping materials shift to left, ascribing that the incorporation of larger ionic radius Mo and Cl elements in the lattice crystal structure can enlarge interplanar spacing.[12] The increasing interplanar spacing further promotes the fasting Li^+ diffusion and enhances the rate performance. Rietveld refinement based on *R-3m* and *C2/m* phase is conducted to accurately analyze the specific changes of lattice parameters after Mo/Cl co-doping and the corresponding results are listed in Figure 1b,c, and Table S1 (Supporting Information). The increasing lattice parameters c of Mo&Cl material in comparison with P0 material demonstrates the expansion of layer spacing, conforming to the left shift of (003) peak.[13] In addition, Mo&Cl material show smaller degree of Li/Ni mixing than P0 material, indicating that the Mo substitution can induce the high ordering structure. Furthermore, the decrease of Li_2MnO_3 content for Mo&Cl material may be ascribed that the generation of Li_2MoO_4 ingredient driving from the reaction between molten MoO_3 and Li_2MnO_3 phase.

© 2024 Wiley-VCH GmbH

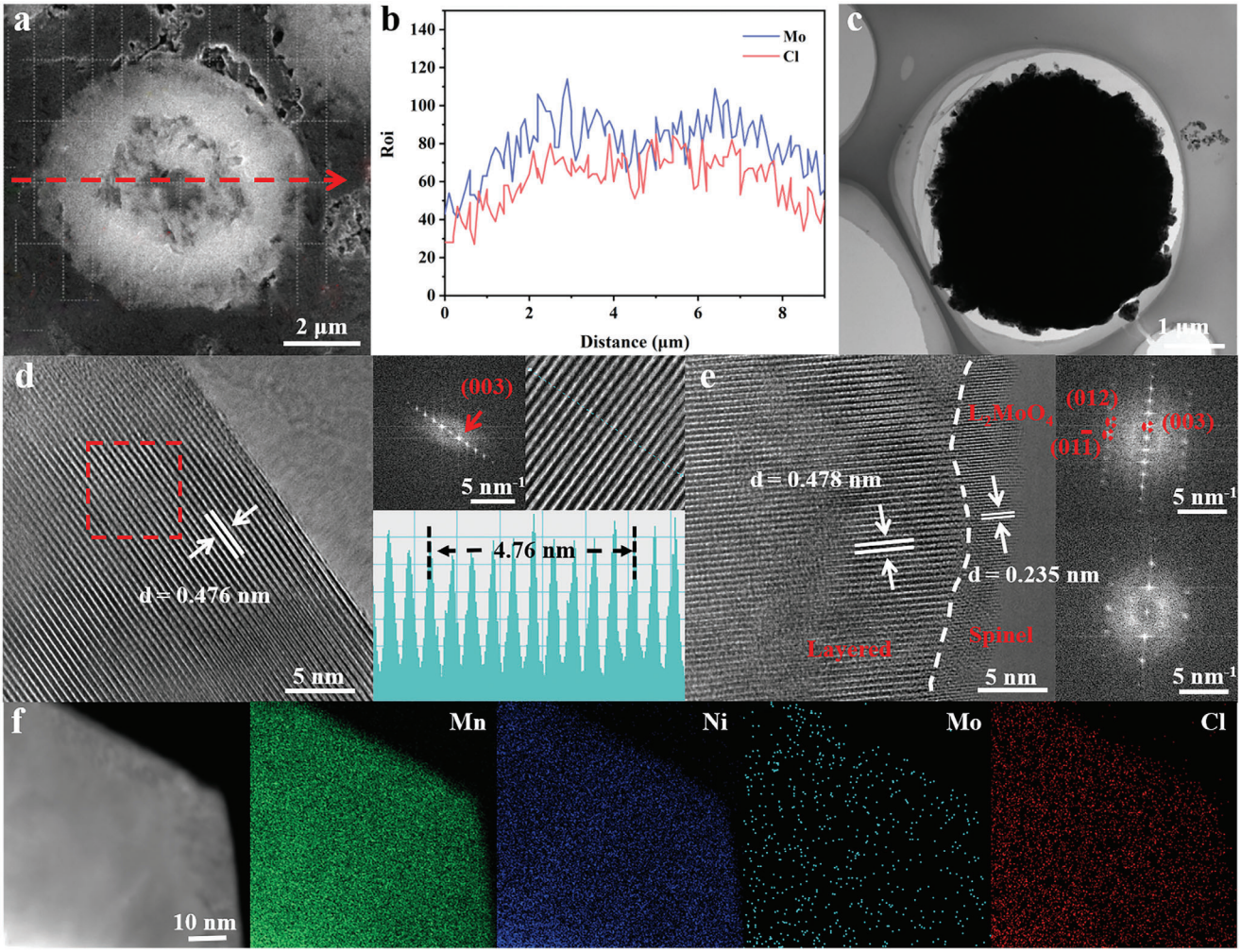


Figure 2. Microstructural structure characterizations of: a) Cross-section SEM image and b) element contents of Mo&Cl material. High-resolution TEM and corresponding FFT patterns for d) P0 and e) Mo&l materials. f) TEM-EDS Mapping images of Mo&Cl material.

Figure 1d,e shows the calculated interslab layer (LiO_2) and slab thickness (MO_2) according to the refined lattice parameters and reported formulas.[14] The corresponding calculated results show that Mo&Cl material possess an enlarged Li^+ layer spacing due to the compression of MO_2 slab and the expansion of c value, which is beneficial for the increasing Li^+ diffusion rate and enhancing the rate capability. Figure 1f shows the Mo 3d and Cl 2p XPS spectra of Mo &Cl material. The obvious peak signals of Mo 3d and Cl 2p peaks located at the range of 228–240 and 195–204 eV, respectively, justify the existence of Mo and Cl on the surface.[15] Besides, the result of energy dispersive spectrometry (EDS) for Mo and Cl material shown in Figure 1g further demonstrates the uniform distribution of Mo and Cl elements. Therefore, these results confirm that Mo/Cl co-doping can induce the variation of crystal structure and the production of new phase Li_2MoO_4. In addition, the enlarged layer interplanar spacing and suppression of Li/Ni mixing will enhance the fast Li^+ kinetics and strengthen the ordering structure of LLOs.

Although above results have successfully demonstrated the existence of dual doping elements on the surface, whether both Mo and Cl elements are incorporated in the bulk structure and their specific influences on the microstructure need to be further explored. Therefore, the cross-section SEM-EDS of Mo and Cl material was first conducted to detect the distribution of doping elements in the bulk structure as shown in **Figures** 2a,b and S3 (Supporting Information). Figure 2b and Figure S3 (Supporting Information) show the changes intensity of EDS line scanning along the central of material and mapping distribution of Mo&Cl elements, respectively. The appearance of weak intensity and uniform distribution Mo/Cl signals perfectly demonstrate the successful bulk element doping, contributing to modulate the crystal structure and coordination environment. In addition, Figure S4 (Supporting Information) displays the FIB-STEM images and the relative EDS mapping of selected region of Mo and Cl material. The formation of some nanopores shown in Figure S4a (Supporting Information) is ascribed to the agglomeration of nanometer primary particle and gas release during the synthesis process[16]. The mapping of Mo and Cl elements in the selected region extending from surface to the bulk exhibit a uniform distribution, further demonstrating the successful doping

 © 2024 Wiley-VCH GmbH

of Mo/Cl in the bulk structure (Figure S4b, Supporting Information). Subsequently, the specific microstructural changes of crystal structure after Mo/Cl co-doping are further analyzed via high-resolution transmission electron microscope (HRTEM) characterization. Clear lattice fringes can be observed for both P0 and Mo&Cl materials as depicted in Figure 2d,e, indicating excellent crystallinity with well-ordered layered structure. The crystal plane spacing of 0.476 nm between the adjacent lattice fringes together with the corresponding fast Fourier transform (FFT) pattern of the red rectangle in Figure 2d all conform to the characteristics of (003) plane of the *R-3m* space group.[17] Carefully compared with P0 material, Mo&Cl material shows an enlarged interplanar spacing with 0.478 nm, ascribing to the increasing electrostatic repulsive interaction and enlarged Li^+ layer spacing.[18] In addition, an obvious epitaxial structure appears on the surface of Mo&Cl material, which is distinct from P0 material. The interplanar spacing 0.235 nm and relative FFT pattern of this epitaxial structure region can match well with the typical characteristics of cubic spinel-like structure.[19] Actually, excess Mo elements will tend to accumulate along the grain boundaries,[20] resulting in the reaction between surface residual lithium and MoO_3 for the formation of Li_2MoO_4 spinel-like phase. Combined with the aforementioned XRD results, we confirm the epitaxial structure is the spinel-like structure Li_2MoO_4 species with Fd-3m space group.[11] Therefore, the enlarged d-spacing and surface spinel-like structure with 3D Li^+ diffusion channels can boost the fast Li^+ kinetics, suppress the irreversible oxygen release, and reduce the interfacial reactions. The TEM-EDS with HAADF images was applied to further detect the microscopic dispersion of Mo and Cl on the primary particle (Figure 2f). The results demonstrate that the dual doping elements can uniformly distribute in the bulk structure of primary particle. Therefore, these results have testified the successful doping of Mo/Cl into the crystal structure and inducing generation of surface spinel-like structure Li_2MoO_4, contributing to stabilize the bulk/surface structure and regulate the local crystal structure and energy band.

The variations of the electronic structure can be explored via XPS and synchrotron X-ray absorption near edge structure (XANES) characterizations. **Figure** 3a,b shows the Mo 3d and Cl 2p XPS spectra at different etching times. Clear signal of Mo 3d and Cl 2p XPS spectra still can be detected with the increasing etching depth, further demonstrating the successful doping of Mo and Cl into the bulk lattice crystal structure. The shift to higher binding energy of the Mn 2p XPS spectra and the reduced splitting energy of Mn 3s spectra after Mo/Cl co-doping as shown in Figure 3c,d, respectively, simultaneously indicate the elevation valence states of Mn. The Mn K-edge X-ray absorption near structure (XANES) is sensitive to the local electronic structure, which can be applied to reflect the valence state and local environment according to the energy position and shape of the absorption edge. Therefore, the Mn K-edge XANES spectra of P0 and Mo &Cl materials are compared in Figure 3e. The Mo and Cl material shows high energy shift in comparison with P0 material, which accurately demonstrates the oxidation of Mn element consistent with the above XPS results. In order to further analyze the influence of Mo/Cl co-doping on the coordination number, bond length, and other details, the Fourier-transform extended X-ray absorption fine structure spectra (EXAFS) at Mn K-edge of P0 and Mo and Cl materials are studied as shown in Figure 3f. Two obvious peaks located at ≈1.5 and ≈2.4 Å in the EXAFS spectra correspond to the oxygen (Mn—O) and metal neighbors (Mn-(Mn, Ni, Li)) in Mn absorb atom, respectively.[21] The EXAFS results confirm that the length of Mn—O bond decreases after Mo/Cl co-doping, suggesting the increasing covalency of the Mn—O bonds. The strong covalent Mn—O band can stabilize the oxidation products O_2^{n-} species of lattice oxygen at high voltage and enhancing the reversible distortions of MnO_6 octahedron, contributing to the reversible anionic redox and strengthening structural stability[18b,22]. In addition, the slight high binding energy shift of Ni 2p XPS peak for Mo&Cl material also indicates the increasing valence of Ni increases after doping (Figure 3g). We speculate that less Mo enters lattice crystal structure in comparison with the Cl substitution, which is ascribed to the accumulation of Mo element in the grain boundaries and subsequent formation of Li_2MoO_4 structure. Therefore, Mn and Ni are oxidized to high valence state for preserving charge neutrality. Besides, the substitution of Mo element possibly induces the generation of $LiMoO_2$ phase due to its multivalence.[23] Therefore, the substitution of Mo^{3+} and the formation of spinel-like structure on the surface cause the increasing Mn valence.[24] The peaks located at ≈ 533.0, 531.5, and 529.5 eV in the O 1s XPS spectra shown in Figure 3h can be assigned to carbonate species, oxygen vacancies, and lattice oxygen, respectively[25]. The content of oxygen vacancies increases after Mo/Cl co-doping, which may be ascribed to the substitution of lattice oxygen with Cl element and the generation of Li_2MoO_4 component. The normalized O K-edge XANES spectra depicted in Figure 3i show two obvious pre-edge peaks located at ≈529.5 eV and 531.5 eV for both P0 and Mo&Cl materials, belonging to the transition of the O 1s electrons to the hybridized O 2p-M 3d orbitals.[26] The decrease of pre-edge peak overall intensity after doping further proves the increased content of oxygen vacancies.[27] Oxygen vacancies are able to enhance electronic conductivity and suppress oxygen release and terrible structural transformation.[28] These results have perfectly demonstrated the influence of Mo/Cl co-doping on the local coordination environment and electronic structure, which is tightly related to the changes in band structure owing to the formation of Mo-O and TM-Cl bands. Moreover, the regulation of band structure will exert a significant influence on the anionic redox activity and electrochemical properties.

The influences of band structure regulation via bulk doping Mo and Cl elements have been successfully characterized from the perspective of the microstructure, local crystal, and electronic structure. Subsequently, the specific influences of band structure regulation on energy storage performance are further analyzed. **Figure** 4a,b shows the initial charge–discharge profiles and relative differential capacity (dQ/dV) profiles at 0.1 C rate (1 C = 250 mAh/g) with the voltage range of 2.0-4.8 V, respectively. A sloped curve below 4.5 V corresponding to the oxidation reaction of Ni^{2+} to Ni^{4+} and an obvious long plateau belonging to the oxidation reaction of O^{2-} to O_2^{n-}/O_2 can be observed for both the two materials.[29] The initial discharge capacity of Mo &Cl materials 234.75 mAh g^{-1} with an initial Coulombic efficiency of 80.77% are higher than those of P0 materials (228.04 mAh g^{-1}, 78.94%), indicating the less oxygen release and enhanced oxygen redox reversibility. The relative dQ/dV curves of initial charge and discharge process can reflect the effects of dual doping elements on the cationic and anionic redox process. Apparently, the

© 2024 Wiley-VCH GmbH

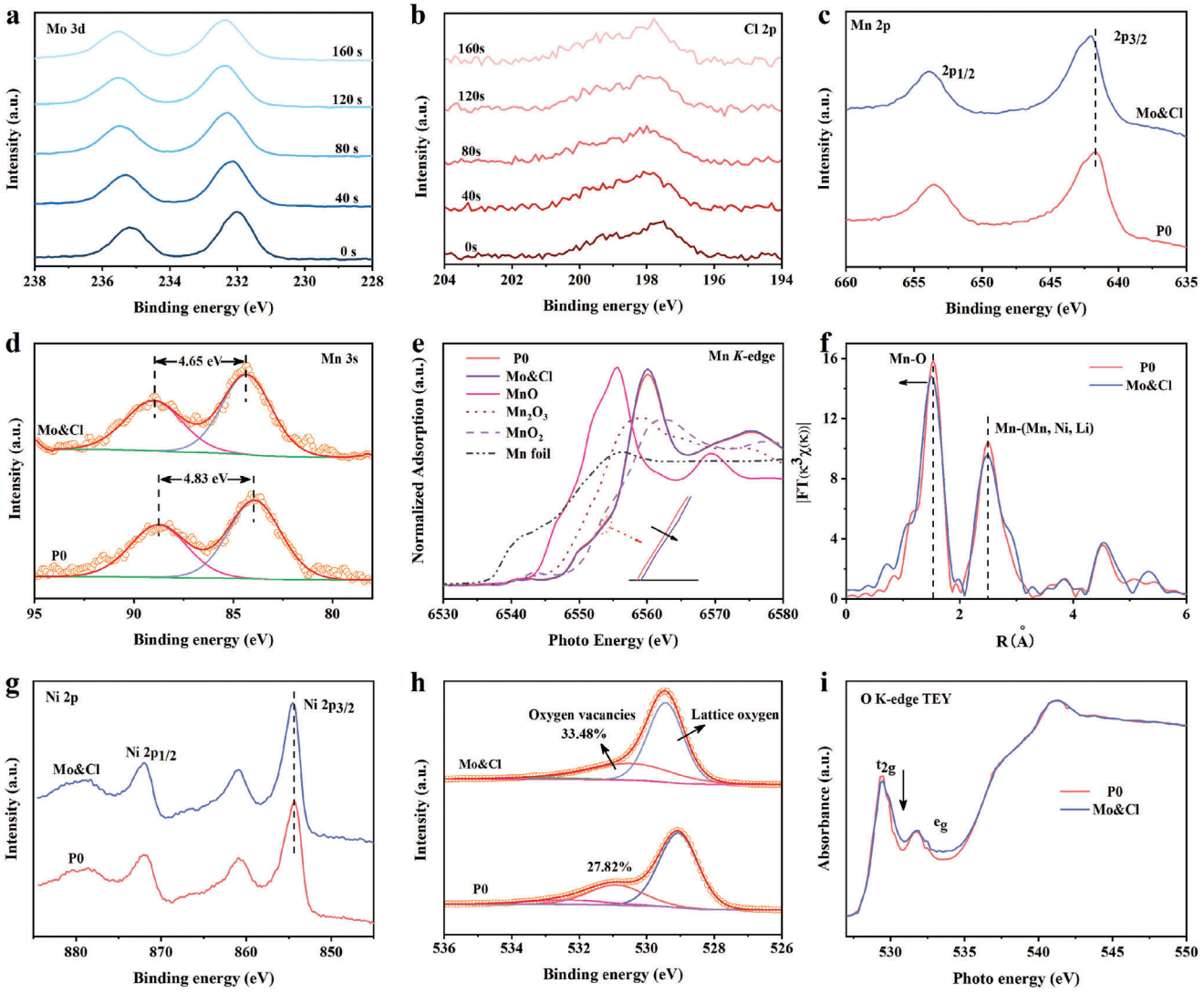


Figure 3. a) Mo 3d and b) Cl 2p XPS spectra of Mo&Cl material at different etching time. c) Mn 2p and d) XPS spectra of P0 and Mo&Cl materials. e) Normalized XANES of Mn K-edge for P0 and Mo and Cl materials. f) Fourier transformed EXAFS spectra at Mn K-edge of P0 and Mo &Cl materials. g) Ni 2p and h) O 1s XPS spectra of P0 and Mo&Cl materials. i) Normalized XANES of O K-edge for P0 and Mo and Cl materials.

oxidation peak of lattice oxygen at ≈4.5 V for Mo&Cl material shifts to low potential in comparison with P0 material, suggesting that band structure regulation can decrease the delithiation potential and enhance the fast kinetics of Li_2MnO_3 activation.[17,18] In addition, the rate capability of Mo&Cl material is also more superior to those of P0 material as shown in Figure 4c: Mo&Cl material still delivers higher reversible capacity (134.94 mAh g^{-1}) than P0 material (120.74 mAh g^{-1}) at 5 C charging and discharging rate. The excellent rate capability of Mo and Cl material can be ascribed to the enlarged Li^+ layer spacing and the existence of fast Li^+ conductive Li_2MoO_4 coating layer. Therefore, the electrochemical impedance spectroscopy (EIS) and galvanostatic intermittent titration technique (GITT) were further carried out to quantitatively calculate the changes in Li^+ diffusion coefficient ($D_{Li}+$). Figure S5a (Supporting Information) shows the Nyquist plots of P0 and Mo&Cl materials. The characteristic curves can be divided into two obvious sections: a semicircle in the high-frequency and a sloping line at the low-frequency area corresponding to charge transfer resistance and the Warburg impedance of Li^+ diffusion process, respectively.[30] Mo&Cl material shows low charge transfer resistance in comparison with P0 material, ascribing that Mo/Cl co-doping can reduce the interfacial resistance and promote fast charge transfer. In addition, the calculated Li^+ diffusion rates of P0 and Mo&Cl materials based on Note S1 (Supporting Information) are 2.063×10^{-14} and 1.381×10^{-14} cm^2 S^{-1}, respectively. What is more, the Li^+ diffusion from the electrode interface to interior of the material is also calculated based on GITT curves (Figure S5b, Supporting Information) and Note S2 (Supporting Information). The average $D_{Li}+$ of Mo&Cl material is also higher than P0 material during the charging process, especially in the stage of anionic redox (Figure S5c, Supporting Information). Therefore, these results successfully demonstrated that Mo/Cl co-doping can accelerate the Li^+ diffusion rate and promote the fast kinetic of

 © 2024 Wiley-VCH GmbH

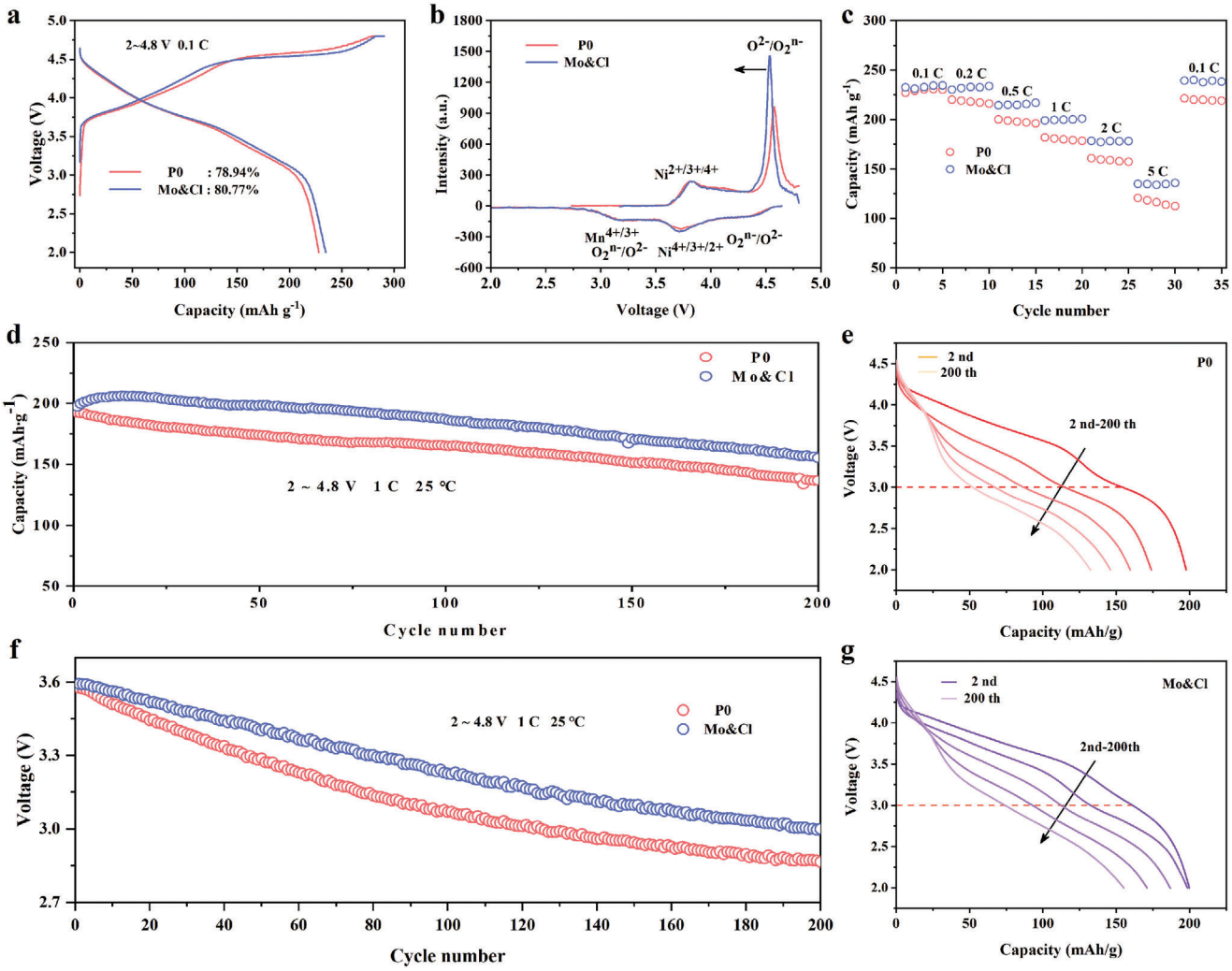


Figure 4. Electrochemical performance of P0 and Mo&Cl materials: a) Initial charge and discharge curves. b) Differential capacity versus potential profiles for the first cycle. c) Rate performance from 0.1 C to 5 C. d) Cycling performance at 1 C for 100 cycles. f) Average voltage performance at 1 C rate for 100 cycles. Discharge curves at different cycles for e) P0 and g) Mo&Cl materials.

anionic redox process due to the increasing d-spacing and existence of surface spinel-like Li_2MoO_4 phase. Figure 4d–f shows the cycling capability of P0 and Mo&Cl materials tested at 1 C rate after 200 cycles. The P0 material can only deliver a low capacity 136.80 mAh g^{-1} with a capacity retention of 71.03%. However, Mo and Cl material still delivers a high capacity 155.15 mAh g^{-1} with an increasing capacity retention of 78.55%. The slow-increasing capacity of Mo&Cl materials during the initial cycles can be ascribed to the electrochemical activation due to the existence of insulating layer Li_2MoO_4[31]. Besides, Mo&Cl material exhibits slower voltage decay in comparison with P0 material. The discharge curves for different cycles for P0 and M0&Cl materials are also applied to analyze the irreversible structural transformation related to the voltage decay (Figure 4e–g). The capacity of P0 material originating from the above 3 V decreases more than Mo&Cl material, indicating the gradual deactivation of Ni and O due to the irreversible structural transformation. Actually, the doping ratio can be continuously optimized for further improving the electrochemical properties. But these results have adequately illustrated that Mo/Cl co-doping can realize the band structure regulation to suppress the oxygen release and the reduction of transition metal ions, contributing to the excellent electrochemical performance.

The enhanced electrochemical performance of LLOs is tightly correlated with the evolution of lattice oxygen and reversibility of anionic redox chemistry. Therefore, ex situ XPS and XAS combining with in situ DEMS shown in **Figure 5** were carried out to reveal the influences of band structure regulation on anionic redox activity during the electrochemical reaction process. Figure 5a,b shows the O 1s XPS spectra of P0 and Mo&Cl materials at 4.8 V charging state and 2.0 V discharging state, respectively. As shown in the O 1s XPS spectra at 4.8 V charging state, the peak at 530.5 eV belongs to the signal of intermediate oxygen due to the oxidization of lattice oxygen (O_2^{n-}, 0<n<2). Its intensity and content can be applied to reflect the activity of anionic redox.[32] Apparently, Mo&Cl materials show more content of intermediate oxygen than P0 materials, indicating the suppressed lattice oxygen loss and enhanced oxygen redox

© 2024 Wiley-VCH GmbH

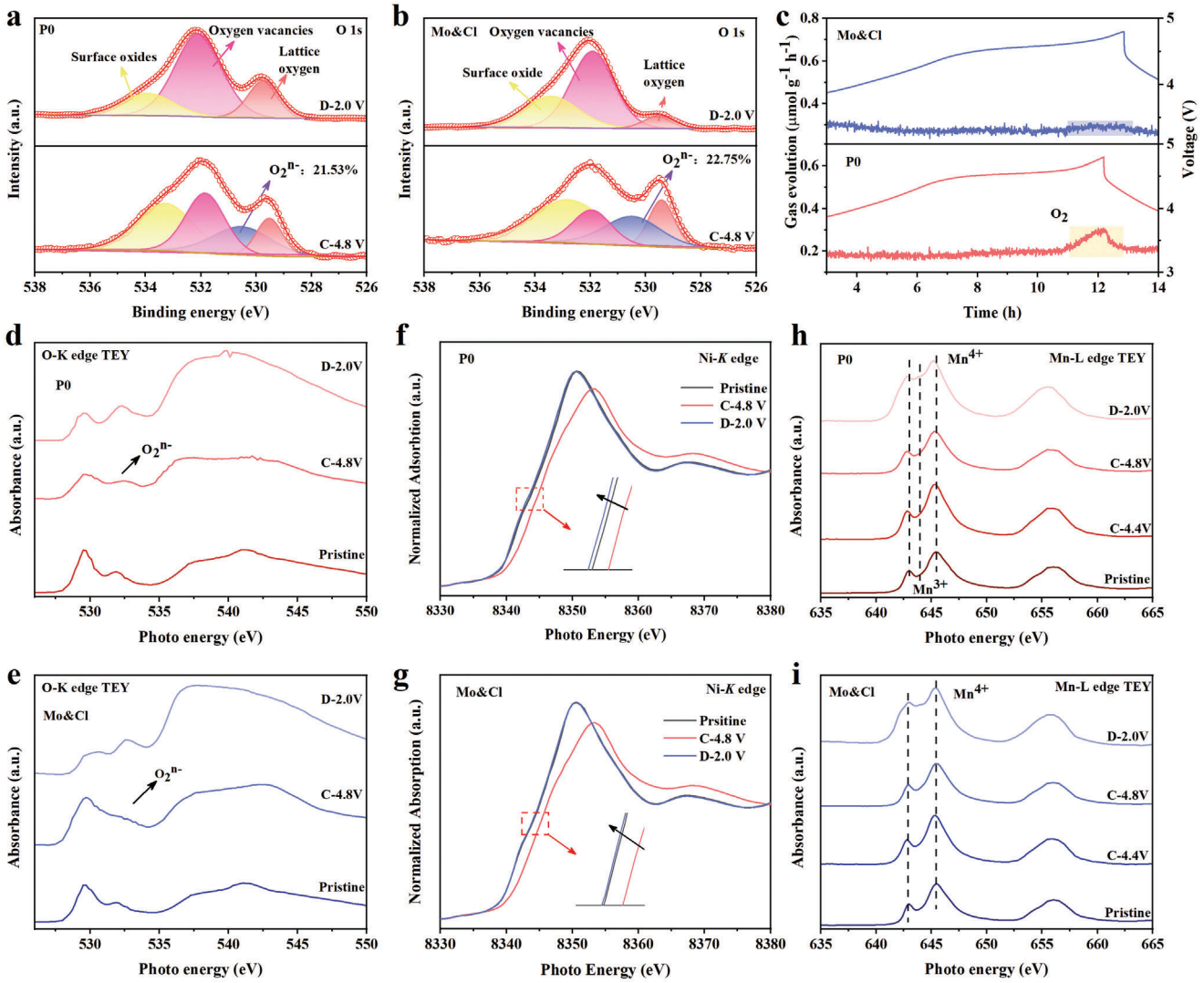


Figure 5. Oxygen evolution and charge compensation mechanism of P0 and Mo&Cl materials: High peak-resolution XPS spectra of O 1s at charging state 4.8 V and discharging state 2.0 V for a) P0 and b) Mo&Cl materials. c) In situ DEMS analysis during charging in the first cycle. Ex situ sXAS spectra of O K-edge for d) P0 and e) Mo&Cl materials. Ex situ Ni K-edge XANES spectra of f) P0 and g) Mo&Cl materials. Ex situ sXAS spectra of Mn L-edge for h) P0 and i) Mo&Cl materials.

reversibility. The DEMS as a powerful characterization is used to directly analyze the conditions of oxygen release for P0 and Mo&Cl materials. The results of Figure 5c show that more oxygen release from P0 material in comparison with Mo&Cl material, indicating that regulated band structure can stabilize the lattice oxygen and suppress the irreversible oxygen release. In addition, epitaxial structure Li_2MoO_4 coating on the surface of Mo&Cl material also contributes to inhibit the release of oxygen to some extent. Figure 5d,e shows the O K-edge sXAS spectra of P0 and Mo&Cl materials at charging and discharging states, the pre-edge region located at the range of 525–534 eV can reflect the hybridization of M 3d and O 2p orbitals. The peaks of ≈529.5 and 532.0 eV belong to the t_{2g} orbitals of M 3d and e_g orbitals of O 2p,[32b] respectively. The additional peak at ≈530.8 eV at 4.8 V charge state is the characteristic signal of anionic redox reaction products (O_2^{n-}),[33] similar to the results of ex situ XPS. Compared with P0 material, the increasing integrated intensity at the low-energy region for Mo&Cl material reflects the enhanced anionic redox activity and stabilization of the O_2^{n-} species,[31,34] which is ascribed that the strengthening covalent of Mn—O or Mo—O bond after energy band modulation can decoordinate with active O_2^{n-} to form stable M—(O—O) bond.[35] In addition, the ex situ Ni K-edge XANES spectra (Figure 5f,g) and Mn L-edge sXAS spectra (Figure 5h,i) were detected to further analyze the changes of electronic structure for transition metal ions during charging and discharging process. As charged to 4.8 V, the Ni K-edge XANES spectra shift to high energy for both P0 and Mo&Cl materials due to the oxidization of Ni element for the charge compensation. However, it is worth noting that Mo&Cl material shows smaller deviation from the initial position than that of P0 material, reflecting the minor Ni reduction due to the suppressed oxygen loss.[33] Two major peaks located at

 © 2024 Wiley-VCH GmbH

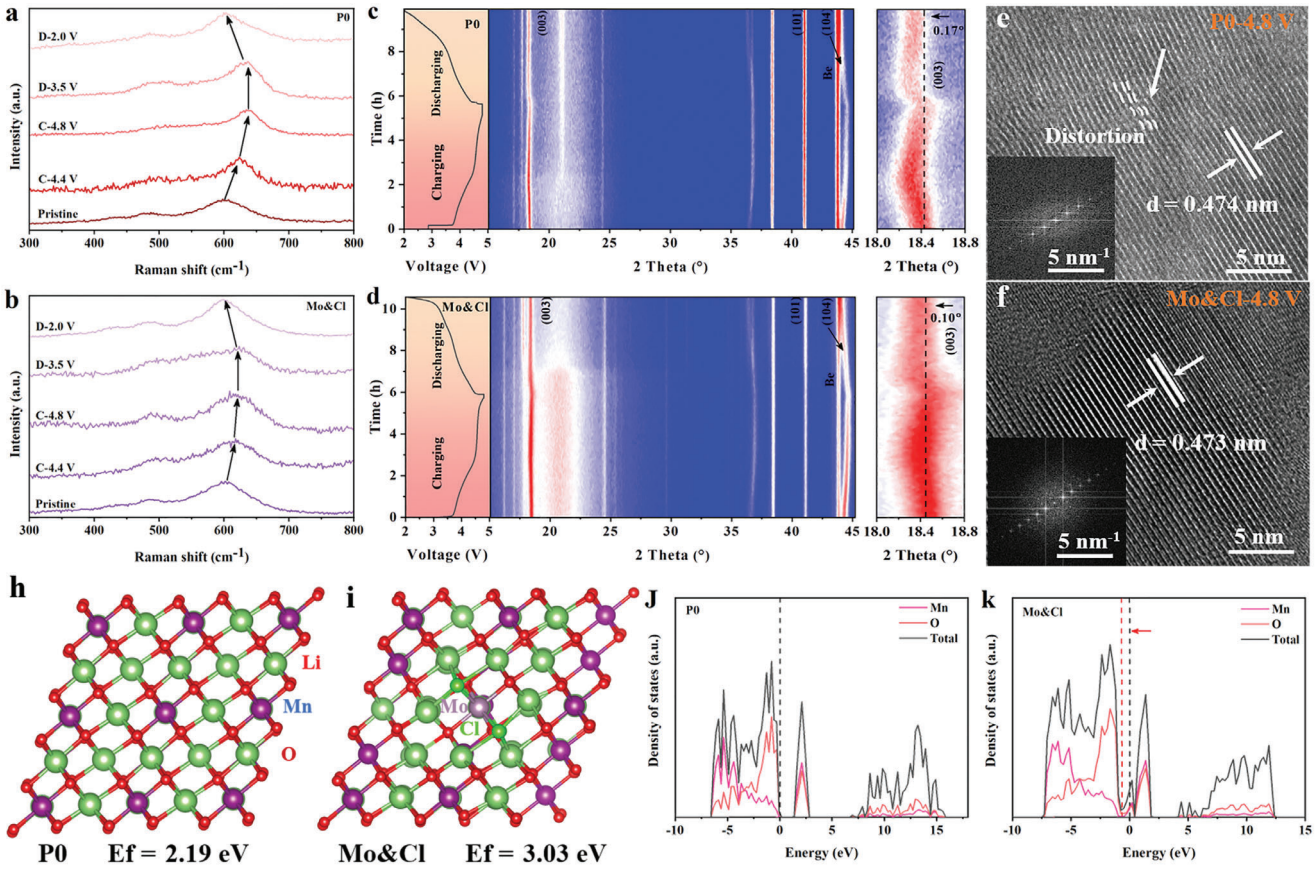


Figure 6. Ex situ Raman spectra of a) P0 and b) Mo&Cl materials. In situ XRD of c) P0 and d) Mo&Cl materials. HRTEM images at charging state 4.8 V for e) P0 and f) Mo&Cl materials. Atomic coordination of h) P0 and i) Mo&Cl materials with one oxygen vacancy at the surface. The density of state of O 2p states, Mn-3d states, and total states in j) P0 and k) Mo&Cl materials.

640–650 eV region of Mn L-edge sXAS spectra represent the Mn^{4+} signal.[32b,36] The low-energy shift of typical Mn^{4+} peak, together with the appearance of Mn^{3+} peak further indicate the reduction of Mn element due to the oxygen loss.[28] However, the Mn^{4+} signal always remains in the initial position for Mo&Cl material during both the charging and discharging process, demonstrating that strong M—O bond strengthens the stability of lattice oxygen and inhibits the oxygen release after band structure regulation. These results have perfectly elaborated that band structure regulation exerts an important effect on anionic redox activity and alleviate the reduction of transition metal ions with the suppressed oxygen loss.

The regulation of band structure on cationic and anionic redox reversibility has been revealed by examining the evolution of lattice oxygen and transition metal ions during cycling. Nevertheless, the structural evolution also need to be further explored after band structure modulation for clarifying the anionic redox regulation mechanism. Therefore, ex situ Raman and in situ XRD analysis were applied to compare the difference of crystal structure between P0 and Mo&Cl materials to elucidate the effects of band structure regulation. **Figure** 6a,b display the results of ex situ Raman. The A_{1g} peak of both two materials shifts to a higher wavenumber during the charging process, ascribing to the shortening of the O—O bond at high voltage and severe distortion of the MnO_6 octahedra during the anionic redox process.[25,37] P0 material shows larger shift than Mo&Cl material, indicating the severe distortion of MnO_6 octahedra and unstable crystal structure. However, the A_{1g} peak of Mo&Cl material is able to restore to the initial position after discharging to 2.0 V, which reflects that regulating the energy band can enhance the reversible distortion of MnO_6 octahedra due to the strengthened covalent M—O bond.[18b] Besides, in situ XRD was also carried out to further investigate the structural evolution of P0 and Mo&Cl materials during the first cycling process and the corresponding contour maps of the XRD results are displayed in Figure 6c,d. The changes of (003) peak position are related to the interplanar space along c-axis and represent the reversibility of structural transformation during cycling. The peak of (003) firstly shifts to left before charging to 4.5 V, ascribing that the extraction of Li^+ can cause the increasing electrostatic repulsive force in the neighboring oxygen slabs and an improvement of lattice constant value c.[38] The (003) peak begins to shift to right as the charging voltage over 4.5 V. Because the oxidization of lattice oxygen for participating in the charging compensation and the induced migration of transition metal ions to lithium layer cause the shrinkage of c-axis and right shift of (003) peak. [39] The (003) peak shifts to low-angle position during the subsequent discharging process, which is ascribed that the intercalation of lithium ions leads to the

© 2024 Wiley-VCH GmbH

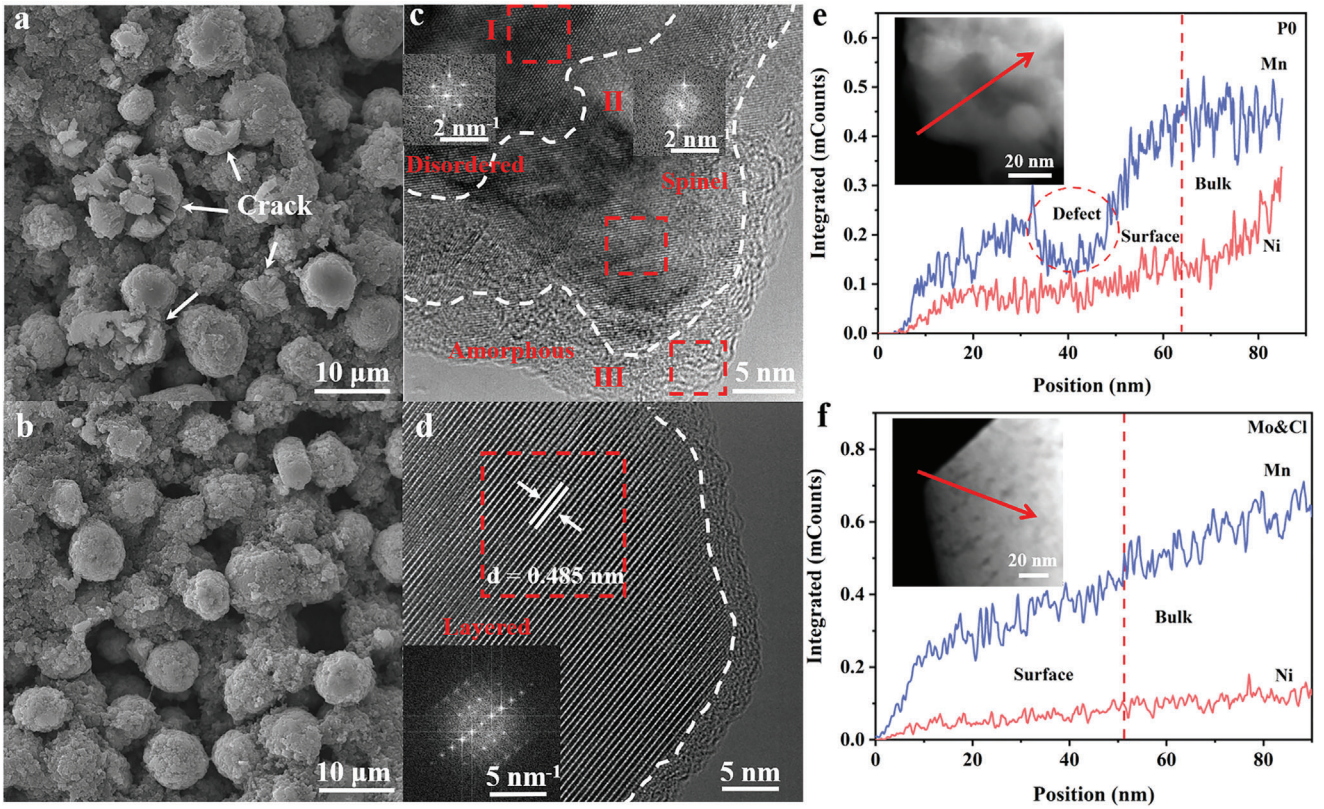


Figure 7. Morphological and structural characterization of cycled P0 and Mo&Cl materials: SEM images of a) P0 and d) Mo and Cl materials. HRTEM images of c) P0 and d) Mo&Cl materials. STEM-EDS line scanning of e) P0 and f) Mo&Cl materials.

weakened electrostatic repulsive force between the neighboring oxygen layer. Although both P0 and Mo&Cl materials show similar variations of (003) peak shift during the first electrochemical activation progress, the overall peak shift of Mo&Cl material is smaller in comparison with P0 material, indicating the suppressed lattice stress, enhanced structural stability and reversibility after the band structure regulation.[40] Figure 6e,f collected HRTEM images of P0 and Mo&Cl materials at charging state 4.8 V. P0 material exhibits some lattice distortion after oxygen redox chemistry. However, Mo&Cl material maintains well-defined layered structures at high voltage. Such phenomena may be ascribed to the dissipation of deleterious strain from lattice contraction after Mo substitution.[41] The strengthened crystal structure stability is beneficial for stabilizing the lattice oxygen and promotes oxygen redox reversibility.[42] Theoretical calculations were applied to better understand the regulation mechanism of anionic redox reversibility from the perspective of band structure modulation. Li_2MnO_3 phase is chosen as the pure model structure for calculating. Mo atom substitutes Mn atom at the transition metal layer and Cl atom substitutes O atom at oxygen layer, forming the dual doping crystal structure (Figure S6, Supporting Information). As shown in Figure 6h,i, Mo&Cl material shows a higher oxygen vacancy formation energy 3.03 eV than that of P0 material (2.19 eV), indicating the increasing lattice oxygen release barrier, restrict oxygen release, and cationic migration due to the formation of strong covalent M—O bond after band structure regulation.[8b,17,43] Figure 6j,k depicts the density of states (DOS) of Mn 3d and O 2p states from first-principles calculations. Compared with P0 material, Mo&Cl material shows a new discrete defect state, benefitting to shorten the band gap and increase the conductivity of Li_2MnO_3 phase.[44] In addition, the non-bonding O 2p band of Mo&Cl material shifts to low energy, demonstrating the increasing charge transfer energy term Δ.[7c,45] What is more, the high d state of Mo element or strong covalent Mo—O or M—Cl bond can decrease the d orbital coulombic interaction term *U* due to the increasing states of filled lower-Hubbard bands (LHB).[46] Therefore, Mo/Cl co-doping can narrow the band gap between *U* and Δ via decreasing the energy level of non-bonding O 2p band and increasing the LHB bands, contributing to the reversible cationic and anionic redox chemistry. Finally, the dual doping strategy conforms to the designing idea of band structure engineering for achieving the reversible anionic redox and strengthening the structural stability, contributing to the aforementioned cycling stability and suppressed voltage decay.

The regulation mechanism of dual doping on the anionic redox reversibility is revealed to mainly change the relative position of non-bonding O 2p and the filled lower-Hubbard bands. The enhanced anionic redox reversibility and suppressed oxygen release will also alleviate the structural deterioration after cycling. Therefore, the specific changes in microscopic structure after 200 cycles are analyzed via SEM and TEM characterizations (**Figure 7**). P0 material shows distinct crack along the whole particle and cause the crush of spherical morphology as shown in Figure 7a, which is ascribed to the continuous oxygen release

 © 2024 Wiley-VCH GmbH

and corrosion of electrolyte. However, Mo&Cl material still obtains the intact secondary spherical morphology due to the stable crystal structure after band structure regulation (Figure 7b). In addition, P0 material also exhibits severe crystal structural degradation in comparison with pristine material in Figure 7c. From the surface to bulk structure, clear amorphous, spinel, and disordered structure can be observed for P0 material. The outside amorphous structure is owing to the continuous interfacial side reactions and electrolyte decomposition induced by oxygen release at high voltage. What is more, oxygen loss leads to the generation of oxygen defects in the lattice structure and cause the easy migration of transition metal ions. Finally, subsequent phase transformation from layered to spinel and disordered rock-salt structure deteriorates the stability of lattice crystal structure and electrochemical properties. In contrast, Mo&Cl material still can keep integral layered structure with clear lattice plane space of 0.485 nm and less amorphous structure on the surface (Figure 7d), ascribed that strong covalent bonding and Li_2MoO_4 coating layered stabilize the oxidation products O_2^{n-}, contributing to suppress lattice oxygen release and irreversible migration of transition metal ions. Moreover, the STEM-EDS line scan results reveal that the intensity of Ni and Mn signals can decrease from the bulk to the surface, reflecting the dissolution of transition metal ions and irreversible lattice oxygen loss to some extent (Figure 7e,f). Compared with Mo&Cl material, the discontinuous change and rapid decreasing intensity of Mn and Ni signal for P0 material are ascribed to the generation of lattice defects and severe dissolution of Mn element after cycling. Furthermore, the dissolution of Ni and Mn elements on the anode electrodes can be further quantitatively compared via the ICP characterization, and the relative results are displayed in Figure S7 (Supporting Information). The surface of the cycled anode electrode for P0 material appears the obvious black substance, which is associated with the dissolution of Mn element (Figure S7a, Supporting Information). However, Mo&Cl material shows less black substance in comparison with P0 material (Figure S7b, Supporting Information). The ICP results of dissolved Mn and Ni elements for P0 material are higher than Mo&Cl material, which is consistent with the above results (Figure S7c, Supporting Information). These results demonstrate that Mo/Cl co-doping can reinforce the stability of crystal structure restrict irreversible phase transformation, alleviate the dissolution of transition metal ions and interfacial side reactions.

3. Conclusion

In summary, we have successfully achieved the regulation of energy bands via Mo/Cl co-doping to promote the anionic redox reversibility and enhance the structural stability of Li-rich layered oxides cathodes. The high d orbital state Mo and low electronegative Cl can selectively substitute the Mn and O atoms to form the strong covalent Mo—O and Mn—Cl bands and alter the band structure: The band energy gap between d orbital coulombic interaction term U and the charge transfer energy term Δ is shortened via increasing the filled lower-Hubbard band (LHB) and decreasing the non-bonding O 2p energy bands, contributing to the enhanced anionic redox reversibility. What is more, the strengthening covalency of Mn—O bond further stabilizes the O_2^{n-} species and enhances the reversible distortion of MnO_6 octahedron, leading to suppress oxygen release and increase structural stability. In addition, the bulk Mo doping and induced epitaxial Li_2MoO_4 can dissipate lattice strain and alleviate the interfacial side reactions. Benefitting from the above, dual doping material delivers increasing cycling stability and excellent rate performance with slow voltage decay. This strategy will provide some references to increase the electrochemical properties of Li-rich layered oxides cathodes from the perspective of the energy band structure regulation strategy.

Supporting Information

Supporting Information is available from the Wiley Online Library or from the author.

Acknowledgements

The authors acknowledge the financial support of Hunan province key R&D technology project (Grant No.2023GK2070). This work was supported by the Beamlines MCD-A and MCD-B (Soochow Beamline for Energy Materials) at the National Synchrotron Laboratory. Besides, we thank the 1W1B beamline of Beijing Synchrotron Radiation Facility (BSRF) for the great help with the XAFS test.

Conflict of Interest

The authors declare no conflict of interest.

Data Availability Statement

The data that support the findings of this study are available from the corresponding author upon reasonable request.

Keywords

anionic redox reversibility, Co-doping, energy band regulation, Li-rich, non-bonding O 2p orbit

Received: February 12, 2024
Revised: March 14, 2024
Published online: March 29, 2024

[1] a) J. H. Song, S. Yu, B. Kim, D. Eum, J. Cho, H. Y. Jang, S. O. Park, J. Yoo, Y. Ko, K. Lee, M. H. Lee, B. Kang, K. Kang, *Nat. Commun.* **2023**, *14*, 4149; b) A. Wang, W. Hong, L. Yang, Y. Tian, X. Qiu, G. Zou, H. Hou, X. Ji, *Small* **2020**, *16*, 2004022; c) S. Li, Z. Luo, L. Li, J. Hu, G. Zou, H. Hou, X. Ji, *Energy Storage Mater.* **2020**, *32*, 306.
[2] S. Jiao, J. Wang, Y.-S. Hu, X. Yu, H. Li, *ACS Energy Lett.* **2023**, *8*, 3025.
[3] a) W. Liu, J. Xu, W. H. Kan, W. Yin, *Small* **2023**, *19*, 2302912; b) M. Z. Qing Zhao, Z. Ye, Y. Li, L. Qiu, Z. Zheng, Y. Liu, B. Zhong, Y. Song, X. Guo, *Nanoscale* **2023**, *15*, 3326.
[4] a) X. Huang, D. Zhang, S. Xu, L. Chen, X. Duan, *Chem. Commun.* **2023**, *59*, 5379; b) Z. Li, H. Li, S. Cao, W. Guo, J. Liu, J. Chen, C. Guo, G. Chen, B. Chang, Y. Bai, X. Wang, *Chem. Eng. J.* **2022**, *452*, 139041; c) J. Chen, H. Chen, Y. Mei, J. Gao, A. Dai, Y. Tian, W. Deng, G. Zou, H. Hou, C. E. Banks, T. Liu, K. Amine, X. Ji, *Energy Storage Mater.* **2022**, *52*, 736.

 © 2024 Wiley-VCH GmbH

[5] a) D. H. Seo, J. Lee, A. Urban, R. Malik, S. Kang, G. Ceder, *Nat. Chem.* **2016**, *8*, 692; b) C. Zhang, B. Wei, M. Wang, D. Zhang, T. Uchiyama, C. Liang, L. Chen, Y. Uchimoto, R. Zhang, P. Wang, W. Wei, *Energy Storage Mater.* **2022**, *46*, 512.
[6] G. Assat, J.-M. Tarascon, *Nat. Energy* **2018**, *3*, 373.
[7] a) X. G. Zhou Xu, W. Song, J. Wang, T. Qin, Y. Yuan, J. Lu, *Adv. Mater.* **2024**, *36*, 2303612; b) H. Wei, Y. Liu, Y. Luo, Y. Huang, L. Tang, Z. Wang, C. Yan, J. Mao, K. Dai, Q. Wu, X. Zhang, J. Zheng, *Adv. Funct. Mater.* **2023**, *34*, 2307583; c) H.-x. Wei, Y.-m. Liu, Yu-h. Luo, Y. Huang, L. Tang, Z. Wang, C. Yan, J. Mao, K. Dai, Q. Wu, X. Zhang, J. Zheng, *Adv. Funct. Mater.* **2023**, 2307583; d) Y. Xie, M. Saubanère, M. L. Doublet, *Energy Environ. Sci.* **2017**, *10*, 266.
[8] a) C. Shen, L. Hu, Q. Duan, X. Liu, S. Huang, Y. Jiang, W. Li, B. Zhao, X. Sun, J. Zhang, *Adv. Energy Mater.* **2023**, *13*, 2302957; b) E. M. M. Saubane're, J.-M. Tarasconab, M.-L. Doublet, *Energy Environ. Sci.* **2016**, *9*, 984.
[9] S. Zhao, K. Yan, J. Zhang, B. Sun, G. Wang, *Angew. Chem., Int. Ed.* **2021**, *60*, 2208.
[10] H. Zheng, Z. Hu, P. Liu, W. Xu, Q. Xie, W. He, Q. Luo, L. Wang, D. Gu, B. Qu, Z.-Z. Zhu, D.-L. Peng, *Energy Storage Mater.* **2020**, *25*, 76.
[11] Z. Zhu, D. Yu, Y. Yang, C. Su, Y. Huang, Y. Dong, I. Waluyo, B. Wang, A. Hunt, X. Yao, J. Lee, W. Xue, J. Li, *Nat. Energy* **2019**, *4*, 1049.
[12] L. Nie, Z. Wang, X. Zhao, S. Chen, Y. He, H. Zhao, T. Gao, Y. Zhang, L. Dong, F. Kim, Y. Yu, W. Liu, *Nano Lett.* **2021**, *21*, 8370.
[13] G. Jia, F. Li, J. Wang, S. Liu, Y. Yang, *ACS Appl. Mater. Interfaces* **2021**, *13*, 18733.
[14] Z. Ding, M. Xu, J. Liu, Q. Huang, L. Chen, P. Wang, D. G. Ivey, W. Wei, *ACS Appl. Mater. Interfaces* **2017**, *9*, 20519.
[15] a) Q. Z. Yao Li, M. Zhang, L. Qiu, Z. Zheng, Y. Liu, Y. Sun, B. Zhong, Y. Song, X. Guo, *ACS Omega* **2023**, *8*, 6720; b) Z. Yu, Q. Lu, Y. Wang, K. Yu, H. Li, X. Yang, Y. Cheng, F. Xu, L. Sun, *Appl. Surf. Sci.* **2023**, *619*, 156683.
[16] a) H. Li, L. Wang, Y. Song, Z. Zhang, A. Du, Y. Tang, J. Wang, X. He, *Adv. Mater.* **2024**, 2312292; b) L. Qiu, M. Zhang, Y. Song, Z. Wu, H. Zhang, W. Hua, Y. Sun, Q. Kong, W. Feng, K. Wang, Y. Xiao, X. Guo, *Angew. Chem., Int. Ed.* **2023**, *62*, 202300209.
[17] P. Yang, S. Zhang, Z. Wei, X. Guan, J. Xia, D. Huang, Y. Xing, J. He, B. Wen, B. Liu, H. Xu, *Small* **2023**, *19*, 2207797.
[18] a) Y. Gao, J. Ma, X. Wang, X. Lu, Y. Bai, Z. Wang, L. Chen, *J. Mater. Chem. A* **2014**, *2*, 4811; b) T. Wang, C. Zhang, S. Li, X. Shen, L. Zhou, Q. Huang, C. Liang, Z. Wang, X. Wang, W. Wei, *ACS Appl. Mater. Interfaces* **2021**, *13*, 12159.
[19] a) D. Luo, X. Ding, J. Fan, Z. Zhang, P. Liu, X. Yang, J. Guo, S. Sun, Z. Lin, *Angew. Chem., Int. Ed.* **2020**, *59*, 23061; b) Q. Luo, Y. Xie, Z. Wu, Q. Xie, D. Yan, H. Zou, W. Yang, S. Chen, *ACS Appl. Energy Mater.* **2021**, *4*, 4867.
[20] D. R. Y. Geon-Tae Park, Un-H Kim, B. Namkoong, J. Lee, M. Wang, A C. Lee, X. Wendy Gu, W C. Chueh, C S. Yoon, Y.-K. Sun, *Energy Environ. Sci.* **2021**, *14*, 6616.
[21] Q. Z. Yaru Yang, J. Yang, H. Liu, Y. Ren, X. Sui, P. Wang, G. Sun, Z. Wang, *Adv. Funct. Mater.* **2023**, *33*, 2304979.
[22] Z. X. Huinan Yu, Z. Xue, Z. Luo, C. Ding, G. Hu, Z. Peng, Y. Cao, K. Du, *J. Mater. Chem. A* **2024**, *12*, 267.
[23] S. Hoshino, A. M. Glushenkov, S. Ichikawa, T. Ozaki, T. Inamasu, N. Yabuuchi, *ACS Energy Lett.* **2017**, *2*, 733.
[24] Z. Ye, B. Zhang, T. Chen, Z. Wu, D. Wang, W. Xiang, Y. Sun, Y. Liu, Y. Liu, J. Zhang, Y. Song, X. Guo, *Angew. Chem., Int. Ed.* **2021**, *60*, 23248.
[25] J. F. Chaoliang Zheng, Z. Wei, D. Zhang, J. Li, *Chem. Eng. J.* **2023**, *467*, 143390.
[26] Z. Feng, H. Song, Y. Li, Y. Lyu, D. Xiao, B. Guo, *ACS Appl. Mater. Interfaces* **2022**, *14*, 5308.
[27] Q. X. Ma, Z. J. Chen, S. W. Zhong, J. X. Meng, F. L. Lai, Z. F. Li, C. Cheng, L. Zhang, T. F. Liu, *Nano Energy* **2021**, *81*, 105622.
[28] X. Gao, H. Zhang, S. Li, S. Zhang, C. Guan, X. Hu, J. Guo, Y. Lai, Z. Zhang, *Adv. Funct. Mater.* **2023**, *33*, 2304065.
[29] a) R. Yu, M. N. Banis, C. Wang, B. Wu, Y. Huang, S. Cao, J. Li, S. Jamil, X. Lin, F. Zhao, W. Lin, B. Chang, X. Yang, H. Huang, X. Wang, X. Sun, *Energy Storage Mater.* **2021**, *37*, 509; b) S. Maiti, H. Sclar, Rosy, J. G, M. Talianker, M. Tkachev, M. Tsubery, X. Wu, M. Noked, B. Markovsky, D. Aurbach, *Energy Storage Mater.* **2022**, *45*, 74.
[30] a) R. X. Chunliu Xu, J. Zhao, F. Ding, Y. Yang, X. Rong, X. Guo, C. Yang, H. Liu, B. Zhong, Y.-S. Hu, *ACS Energy Lett.* **2022**, *7*, 97; b) J. L. Longcheng Zhang, L. Yue, Z. Xu, K. Dong, Q. Liu, Y. Luo, T. Li, X. Cheng, G. Cui, Bo Tang, A. A. Alshehri, K. A. Alzahrani, X. Guo, X. Sun, *Nano Res.* **2022**, *15*, 304.
[31] Q. Shao, P. Gao, C. Yan, M. Gao, W. Du, J. Chen, Y. Yang, J. Gan, Z. Wu, C. Zhang, G. Chen, X. Zheng, Y. Lin, Y. Jiang, W. Sun, Y. Liu, M. Gao, H. Pan, *Adv. Mater.* **2022**, *34*, 2108543.
[32] a) Y. Yang, C. Gao, T. Luo, J. Song, T. Yang, H. Wang, K. Zhang, Y. Zuo, W. Xiao, Z. Jiang, T. Chen, D. Xia, *Adv. Mater.* **2023**, *35*, 2307138; b) Y. Fan, E. Olsson, G. Liang, Z. Wang, A. M. D'Angelo, B. Johannessen, L. Thomsen, B. Cowie, J. Li, F. Zhang, Y. Zhao, W. K. Pang, Q. Cai, Z. Guo, *Angew. Chem. Int. Ed. Engl.* **2022**, *62*, 202213806.
[33] E. Wang, D. Xiao, T. Wu, X. Liu, Y. Zhou, B. Wang, T. Lin, X. Zhang, H. Yu, *Adv. Funct. Mater.* **2022**, *32*, 2201744.
[34] E. Wang, D. Xiao, T. Wu, B. Wang, Y. Wang, L. Wu, X. Zhang, H. Yu, *Battery Energy* **2023**, *2*, 20220030.
[35] F. N. Huaifang Shang, B. Li, Y. Zuo, S. Lu, D. Xia, *ACS Appl. Mater. Interfaces* **2018**, *10*, 21349.
[36] T. Jenkins, J. A. Alarco, B. Cowie, I. D. R. Mackinnon, *J. Mater. Chem. A* **2022**, *10*, 24487.
[37] Y. Zhang, Z. Chen, X. Shi, C. Meng, P. Das, S. Zheng, F. Pan, Z. S. Wu, *Adv. Energy Mater.* **2022**, *13*, 2203045.
[38] J. Li, J. Zhao, C. Tang, T. Jia, J. Hou, C. Cao, Y. Zhu, *J. Power Sources* **2021**, *511*, 230427.
[39] a) G. Zhou, D. Zhang, Y. Zhang, W. Wang, T. Uchiyama, C. Zhang, Y. Uchimoto, W. Wei, *ACS Appl. Mater. Interfaces* **2023**, *15*, 19055; b) J. D. Hualong Wu, Y. Zhang, L. Lin, G. Gao, T. Li, X. Yi, B. Sa, J. Wang, L. Wang, J. Li, K. Amine, D.-L. Peng, Q. Xie, *Adv. Funct. Mater.* **2023**, *33*, 2303707.
[40] D. J. Haotian Dong, S. Xing, L. Zhao, L. Hu, J. Mao, H. Zhang, *Small* **2023**, 2307156.
[41] G.-T. Park, B. Namkoong, S.-B. Kim, J. Liu, C. S. Yoon, Y.-K. Sun, *Nat. Energy* **2022**, *7*, 946.
[42] Z. Hao, H. Sun, Y. Ni, G. Yang, Z. Yang, Z. Hao, R. Wang, P. Yang, Y. Lu, Q. Zhao, W. Xie, Z. Yan, W. Zhang, J. Chen, *Adv. Mater.* **2023**, *36*, 2307617.
[43] Y. Q. Xiaoyu Zhang, S. Guo, K. Jiang, S. Xu, H. Xu, P. Wang, P. He, H. Zhou, *Adv. Mater.* **2019**, *31*, 1807770.
[44] J. Xu, J. Wan, W. Zhang, Y. Li, F. Cheng, Z. Cheng, Y. Xu, S. Sun, Q. Li, C. Fang, J. Han, *Adv. Funct. Mater.* **2023**, *33*, 2214613.
[45] T. A. Wynn, C. Fang, M. Zhang, H. Liu, D. M. Davies, X. Wang, D. Lau, J. Z. Lee, B.-Y. Huang, K.-Z. Fung, C.-T. Ni, Y. S. Meng, *J. Mater. Chem. A* **2018**, *6*, 24651.
[46] Q. Li, Ning, D. W, K. An, Y. Tang, D. Zhou, G. Schuck, Z. Chen, N. Zhang, X. Liu, *Nat. Commun.* **2022**, *13*, 1123.

 © 2024 Wiley-VCH GmbH